Proceedings of the ASME 2015 International Mechanical Engineering Congress and Exposition
IMECE2015
November 13-19, 2015, Houston, Texas

IMECE2015-50174

MODELING LASER TRAVEL AND ITS EFFECTS ON THERMAL STRESSES IN LASER HARDENING OF STEEL

Suhash Ghosh
University of Hartford
West Hartford, CT, USA

Chittaranjan Sahay
University of Hartford
West Hartford, CT, USA

Devdas Shetty
School of Engineering and Applied Sciences
University of the District of Columbia
Washington DC, USA

ABSTRACT

To achieve a precise and controlled laser process, a thorough analysis of the thermal behavior of the material is necessary. The knowledge of the thermal cycles is important to ascertain suitable processing parameters, thus improving surface properties when the alloys are laser irradiated. In the present paper, a numerical simulation of the laser hardening process has been developed using the finite element (FE) code ABAQUS™ to solve the heat transfer equation inside the treated material (AISI 4140 steel). The thermal analysis is based on Jaeger's classical moving heat source method by considering the laser beam as a moving plane (band/disc) heat source and the target material is a semi-infinite solid. However, the FE model, used to solve the governing equation, does not directly accommodate the moving nature of heat source. A reasonable approximation is to divide the laser travel on the substrate into many small time/load steps, and apply variable flux and boundary conditions in each time/load step. This approximates the quasi-steady state phenomena over the series of these time steps for the complete laser travel. This paper investigates the effects of the choice of time/load steps on the temperature and thermal stress evolution as well the computing times in the process.

INTRODUCTION

Laser hardening has shown itself to be an increasingly popular method to achieve selective hardening of materials to enhance the mechanical properties, in particular wear [1,2] and fatigue resistance of steels [3,4]. The advantage of using a laser for surface processing arises from its highly directional nature and the ability to deliver controlled amounts of energy to the desired regions [5]. Treatment depth is accurately controlled and highly reproducible. Additionally, significantly high hardness can be achieved [6,7]. This is accomplished by applying the laser beam to the selected area where it introduces a large amount of heat to the surface of the material very rapidly. As the heat is introduced rapidly and only locally under the beam when the beam is switched off or moved away from the targeted area the bulk of the surrounding material acts as a heat sink and removes the heat almost as rapidly as it was added. Provided that the targeted area at the surface was heated sufficiently the high rate of heat diffusion into the surrounding material once the laser is removed makes the process essentially self-quenching allowing hardening to occur [6,7].

Many papers [8-14] have discussed the theory of laser transformation hardening in hypo-eutectoid steels. These models predict the temperature evolution, transient behavior of thermal stress, temperature history based material solid-state phase transformations, hardness, hardness depth, and finally, the residual stress formation as a complex coupling action of phase transformations and thermal stresses. The commonly used strategy is to first obtain temperature results from the temperature elements in a thermal loading model, followed by the calculations of thermal stresses from the structural elements under structural loading (including temperatures from the first model). In a sequentially coupled temperature-stress analysis, a transient thermal analysis is first performed to determine the temperature history in the work piece. As discussed by Ghosh et al. [15], this would need the temperature dependent material properties like, density, specific heat, conductivity and latent

heat as inputs. In many cases, the temperature history is then extracted and used by a kinetic model that uses a much finer mesh by interpolating in space. This model tracks the austenite formation and calculates the phase fractions formed while cooling. Thermal stresses are calculated using a standard input file that is sequentially coupled to the temperature history obtained earlier. The phase fractions obtained from the finite difference kinetic model are then coupled to the thermal stress history to calculate strain terms related to transformation plasticity and volume change. When added to the subtotal of elastic, plastic and thermal stresses, they would determine the residual stresses in the workpiece.

It is not clearly written in any of these articles what modeling strategies were used to simulate the laser motion. It is quite intuitive that the time step selection, and the corresponding step-over distance, based on the laser travel speed would affect the temperature evolution and the associated stresses. However, no prior work in this area or any systematic numerical study related to moving heat source problems could be found in the literature. To the best of knowledge of the authors, this paper is a novel and first ever attempt in this focus area.

When utilizing a finite element approach, the commonly used strategy is to first obtain temperature results from the temperature elements in a thermal loading model based on the heat diffusion equation [16]

$$\nabla\left(k\nabla T\right)+\dot{q}=\rho c_p\frac{\partial T}{\partial t} \tag{1}$$

where the left side of the equation represents the heat diffusion in each direction, k being the thermal conductivity (W/m-K), T the temperature (K) and the heat generation rate, $\dot{q}$ (W/m^3) while the right side of the equation represents the energy storage with density, ρ (kg/m^3), specific heat, c_p (J/kg-K) and time, t (s). In this process, no heat generation was used. The following equations were used as boundary conditions. Equation (2) is used for flux (Φ) underneath the laser as it traverses the plate, while equation (3) is used on the rest of the surfaces for natural convection with the ambience temperature T_0 assumed to be at 25°C. h is the heat transfer coefficient taken as about 5 W/m^{2}K (natural cooling).

$$-k\nabla T=\Phi \tag{2}$$

$$-k\nabla T=-h\left(T-T_0\right) \tag{3}$$

$$-k\nabla T=\varepsilon\sigma\left(T^4-T_0^4\right) \tag{4}$$

The heated surface elements will also dissipate heat through radiation into the surrounding. Equation (4) is a significant component especially for the track irradiated by the laser on the plate. ε is the emissivity of the selected plate material, while σ is the Stefan-Boltzmann constant [5.67x10^{-8} W/m^{2}K^4].

FINITE ELEMENT MODELS

A total of five different models, based on strategies to model laser travel, were created using ABAQUS 6.5. For thermal analysis DC3D8 (DOF Temperature) element was selected. This could be then converted to C3D8 (DOF displacement in X, Y, and Z) for the structural analysis.

Three different mesh sizes were used, a fine mesh of 0.25mm, a medium mesh of 0.5mm, and coarse mesh of 1mm. When selecting the mesh size it is important to balance the need of a finer mesh for greater accuracy in the results with the increase in computational time and resources required to utilize it. This is especially important if the geometry of the spot is not rectangular because if the mesh is too coarse it may require the shape of the spot to be distorted to a degree that would affect the results. The computational times for both thermal and stress analysis for the medium mesh were way too high as compared to coarse mesh. Additionally, a maximum difference of only 3% in the temperature (maximum at any node) were observed. The simulations for fine mesh size of 0.25 mm could not be completed due to limited computational resources; both in processor speed (Core-2 Duo 1.8 GHz) and RAM (2 GB). To maintain the brevity of the paper, and to focus only on the comparative study of different methods of modeling/simulating the laser travel, coarse mesh of 1mm was used in all models. Selection of a relatively coarse mesh for all five modeling strategies enable comparing results for temperature at nodes and total computational times in all cases with a high degree of confidence. This further enables the user to settle on a trade-off between accuracy and simulation run times. A total of 8725 nodes and 7200 elements were used.

A similar model with a uniform intensity circular beam was validated by Ghosh *et al.* [17] in their earlier work with the results of the experimental setup of Safdar *et al.* [18]. The authors in this paper feel that the validation for a rectangular beam (used in this paper) is not necessary here. Additionally, the comparison between five different modeling strategies in this paper is entirely based on the same fundamental model, hence, any error associated with the model equally weighs out (normalize) in each strategy.

The program automatically interpolates the temperature as necessary. Since the temperature change is very rapid during the initial heating, a smaller time increment is necessary for convergence as compared to the time increment required for convergence during slow cooling process when the laser goes past the workpiece. The thermo-mechanical properties (density, specific heat and thermal conductivity) were obtained from reference [19].

The models simulated a rectangular laser beam of size 12x8 mm traversing a flat plate of dimensions 50x50x18 mm at room temperature (20°C). The laser traversed the length of the plate right through the center line of the plate. The beam is assumed to have uniform power intensity (top hat profile). The

laser power into the plate was assumed to be 1000W (absorptivity of 0.85) and the speed of the laser was 2mm/s. The path of the laser was 50mm long following the centerline of the plate with the laser being symmetric about the centerline of the plate. This is shown in figure 1.

The motion of the beam was modeled by applying a heat flux on the surface (specific element face) of the elements that would fall under it at a given time. The flux was then shifted over to the next rows of elements along the leading edge of the beam after the time it would take the beam to travel across those many elements had elapsed, while the same number of elements was removed from the elements along the trailing edge, as shown in figures 2 through 6. This procedure was iterated as many times as were required for the flux representing the beam to completely traverse the 50mm long path.

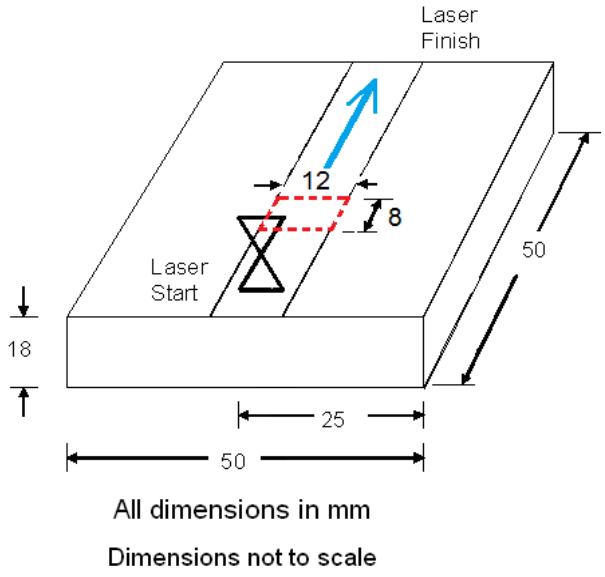

Figure 1. Schematic of the Plate Laser Hardening

Strategy #1: As shown in figure 2, no overlap of laser flux in consecutive time steps was considered. Hence each time/load step was 4 seconds. Hence, the total travel of 50mm was completed in 6 time/load steps of 4 seconds each and a 7th time/load step of 1 second. The plate was allowed to cool down for an additional 155 seconds without any laser flux applied.

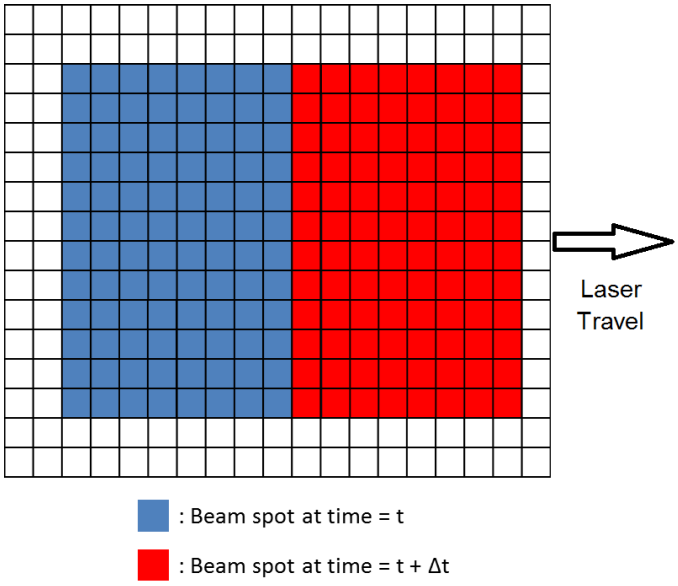

Figure 2. Motion Diagram of Heat Flux for Strategy #1.

Strategy #2: As shown in figure 3, 25% overlap of laser flux in consecutive time steps was considered. Hence each time/load step was 3 seconds. Hence, the total travel of 50mm was completed in 8 time/load steps of 3 seconds each and a 9th time/load step of 1 second. The plate was allowed to cool down for an additional 155 seconds without any laser flux applied.

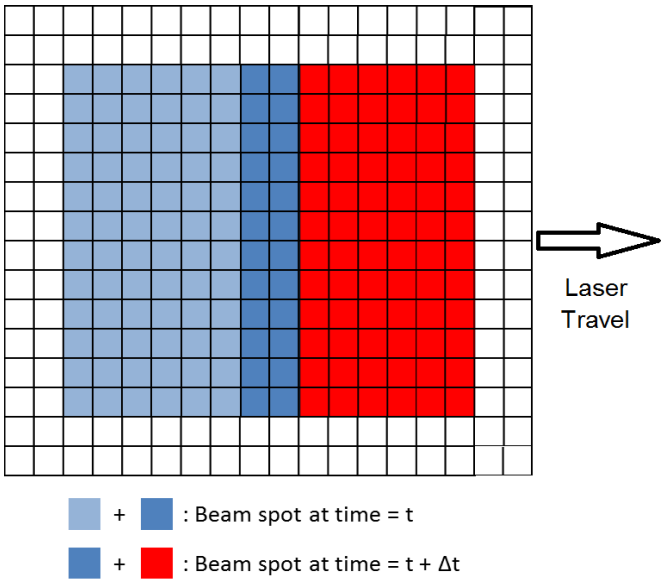

Figure 3. Motion Diagram of Heat Flux for Strategy #2.

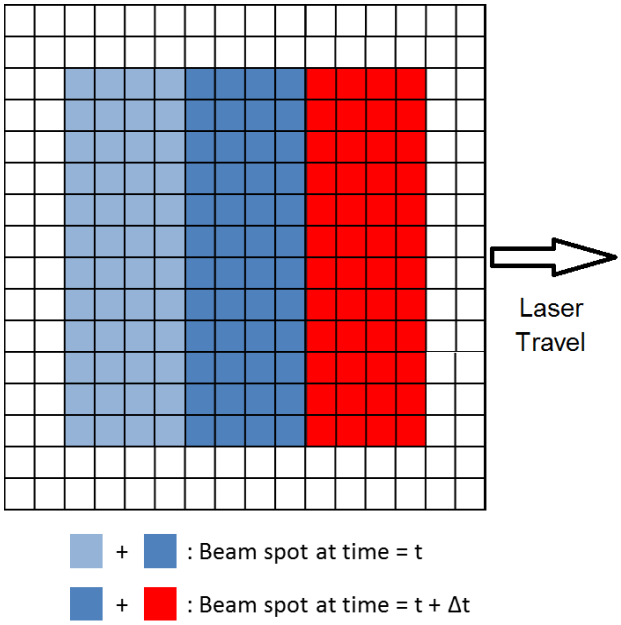

Figure 4. Motion Diagram of Heat Flux for Strategy #3.

Strategy #3: As shown in figure 4, 50% overlap of laser flux in consecutive time steps was considered. Hence each time/load step was 2 seconds. Hence, the total travel of 50mm was completed in 12 time/load steps of 2 seconds each and a 13th time/load step of 1 second. The plate was allowed to cool down for an additional 155 seconds without any laser flux applied.

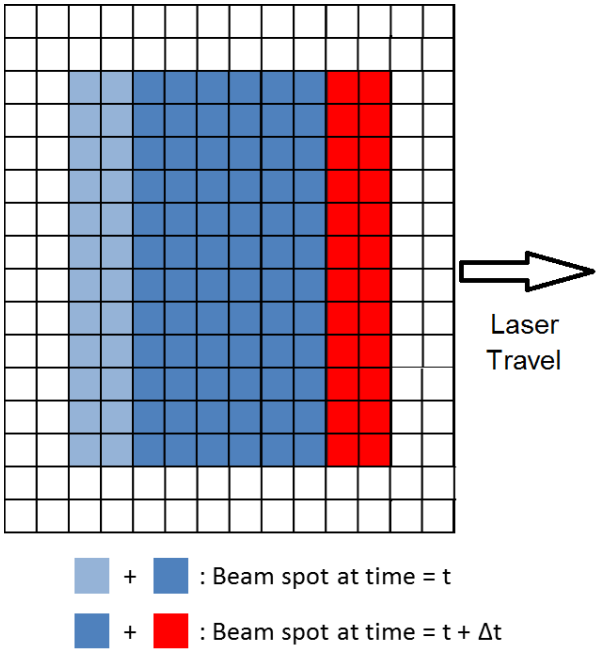

Figure 5. Motion Diagram of Heat Flux for Strategy #4.

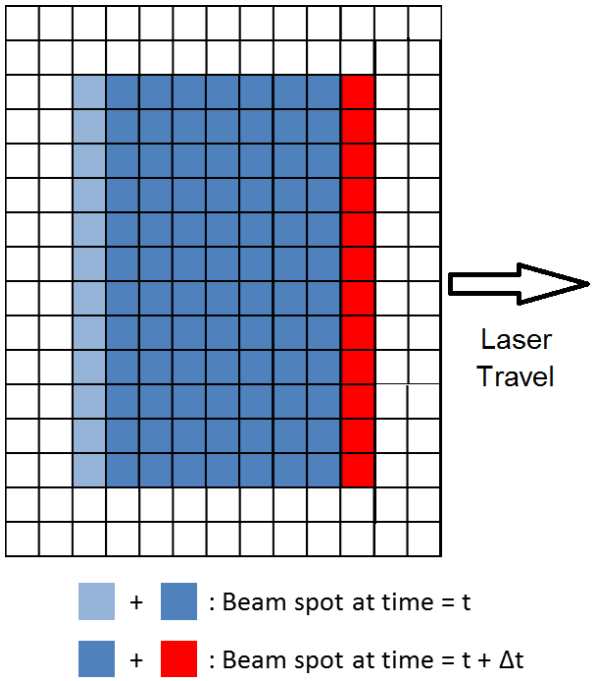

Figure 6. Motion Diagram of Heat Flux for Strategy #5.

Strategy #4: As shown in figure 5, 75% overlap of laser flux in consecutive time steps was considered. Hence each time/load step was 1 seconds. Hence, the total travel of 50mm was completed in 25 time/load steps of 1 second each. The plate was allowed to cool down for an additional 155 seconds without any laser flux applied.

Strategy #5: As shown in figure 6, 87.5% overlap of laser flux in consecutive time steps was considered. Hence each time/load step was 0.5 seconds. Hence, the total travel of 50mm was completed in 50 time/load steps of 0.5 seconds each. The plate was allowed to cool down for an additional 155 seconds without any laser flux applied.

RESULTS AND DISCUSSION

The simulations were run successfully for the five original models. The models yielded some interesting results to compare between them. As shown in figure 7, three transverse sections (planes perpendicular to the laser travel direction and the top surface of the plate) were considered for temperature and thermal stress studies. On each section several nodes were studied for comparison of temperatures calculated in the five strategies.

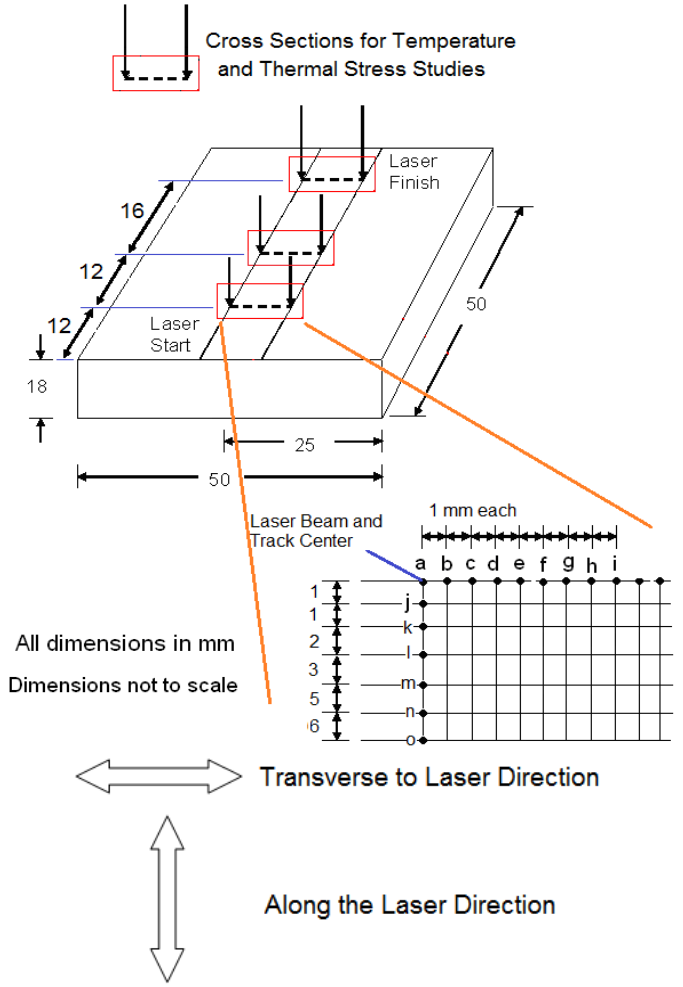

Figure 7. Schematic of Transverse Sections and Locations of Survey Points.

Ghosh *et al*. [17] have reported in their earlier work that strategy #5 returns temperatures that match closely with experimental readings. In fact, the lowest time/load step can only be achieved in this strategy. Hence, for the work reported in this paper, strategy #5 will be taken as the baseline for comparisons with the other strategies.

Figures 8 through 10 show the variation of temperature on the survey points (a, b, c, d, e, f, g, h and i) on the plate surface in the transverse direction to the laser traverse on sections that are at 12mm, 24 mm and 40 mm away from the starting plate edge (front edge in figure 7), respectively. Figures 11 through 13 show the variation of temperature on the survey points (a, j, k, l, m, n and o) in the depth direction on the sections that are at 12mm, 24 mm and 40 mm away from the starting plate edge (front edge in figure 7), respectively, in the transverse direction to the laser traverse. Since the nodal temperatures are symmetric about the plane of center track (normal to the plate top surface) only half plate nodal temperatures at the survey sections have been reported in these figures. Also, the shown temperatures are the maximum at the respective nodes for the complete travel of the laser. As expected, the temperatures are highest at the laser track center, and it drops consistently away from the center line. Although the rectangular half-beam width was 6mm, not all of it results in a reasonable microstructural change. For example, a normalized AISI 4140 steel has an AC1 temperature of nearly 1000 K and AC3 temperature of about 1110 K. For any tangible change of microstructure (consequently, hardness) a minimum temperature of 1000 K must be reached at the node. With this scale, an approximate width and depth of hardening can be determined.

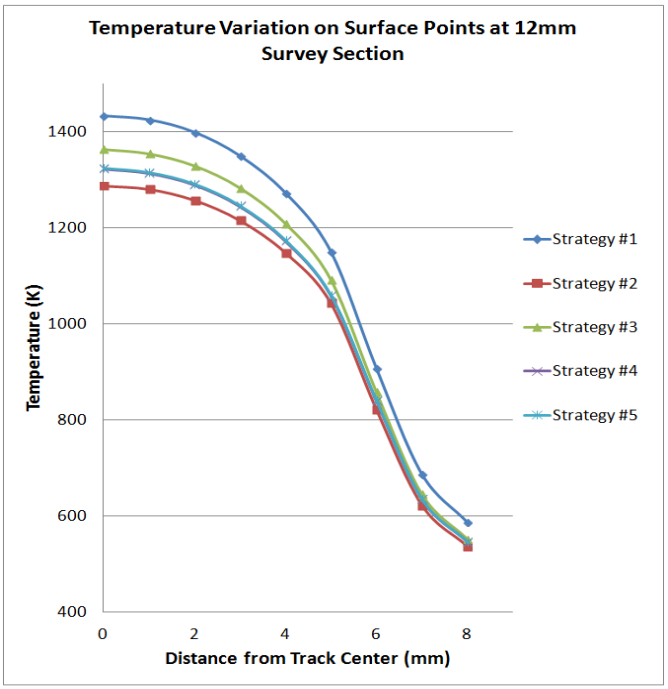

Figure 8. Temperature Variation on Surface Points at 12mm Survey Section.

Figure 8 shows that the strategy #1 results in the highest temperatures and Strategy #2 the lowest temperatures at all nodes at section 12mm. interestingly, the other strategies result in values between the two. This is because the 12 mm section lies at the interface of the consecutive flux steps in strategy #2, while the section lies either in the middle or close to the middle of the successive flux steps in the other strategies. It can also be observed that strategies #3 and #4 reported almost similar results for all nodes. With strategy #5 as the baseline model, on the 12mm section, a maximum difference of 0.18% for strategy #4, 3% for strategy #3, 2.8% for strategy #2, and 8.5% for strategy #1 was calculated.

Figure 9 shows that the strategy #1 results in the lowest temperatures and Strategy #3 the highest temperatures at all nodes at section 24mm. The other strategies result in values between the two. This is because the 24 mm section lies at the interface of the consecutive flux steps in strategy #1, while the section lies either in the middle or close to the middle of the successive flux steps in the other strategies. It can also be observed that strategies #3, #4 and #5 reported almost similar results for all nodes. With strategy #5 as the baseline model, on

the 24mm section, a maximum difference of 0.62% for strategy #4, 1.5% for strategy #3, 4.9% for strategy #2, and 24.4% for strategy #1 was calculated.

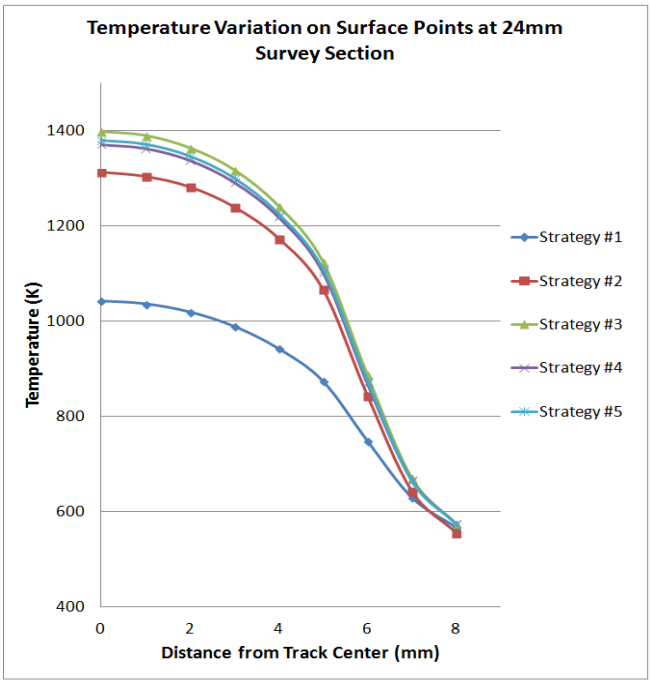

Figure 9. Temperature Variation on Surface Points at 24mm Survey Section.

Figure 10 shows that strategy #1 results in the lowest temperature and strategy #2 the highest temperature at all nodes at section 40mm. The other strategies result in values between the two. This is because the 40 mm section lies at the interface of the consecutive flux steps in strategy #1, while the section lies either in the middle or close to the middle of the successive flux steps in the other strategies. It can also be observed that strategies #3, #4 and #5 reported almost similar results for all nodes. With strategy #5 as the baseline model, on the 40mm section, a maximum difference of 1% for strategy #4, 1.7% for strategy #3, 3.5% for strategy #2, and 22.7% for strategy #1 was calculated.

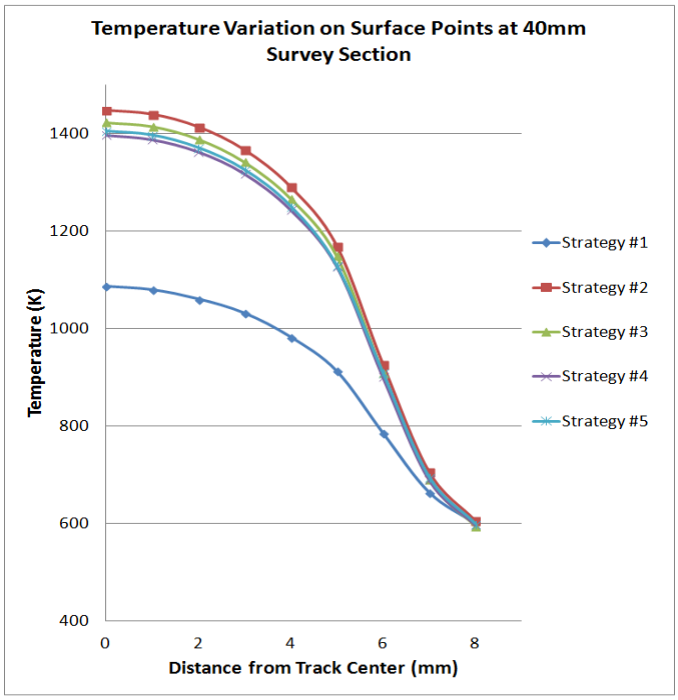

Figure 10. Temperature Variation on Surface Points at 40mm Survey Section.

The variations along the depth on the same survey sections are similar. Figure 11 shows that the strategy #1 results in the highest temperatures and Strategy #2 the lowest temperatures at all nodes at section 12mm. This is because the 12 mm section lies at the interface of the consecutive flux steps in strategy #2, while the section lies either in the middle or close to the middle of the successive flux steps in the other strategies. It can also be observed that strategies #3 and #4 reported almost similar results for all nodes. With strategy #5 as the baseline model, on the 12mm section, a maximum difference of 0.9% for strategy #4, 3.3% for strategy #3, 4.8% for strategy #2, and 9.9% for strategy #1 was calculated. Figure 12 shows that the strategy #1 results in the lowest temperatures and Strategy #3 the highest temperatures at all nodes at section 24mm. The other strategies result in values between the two. It can also be observed that strategies #3, #4 and #5 reported almost similar results for all nodes. With strategy #5 as the baseline model, on the 24mm section, a maximum difference of 0.76% for strategy #4, 1.5% for strategy #3, 5.15% for strategy #2, and 24.4% for strategy #1 was calculated.

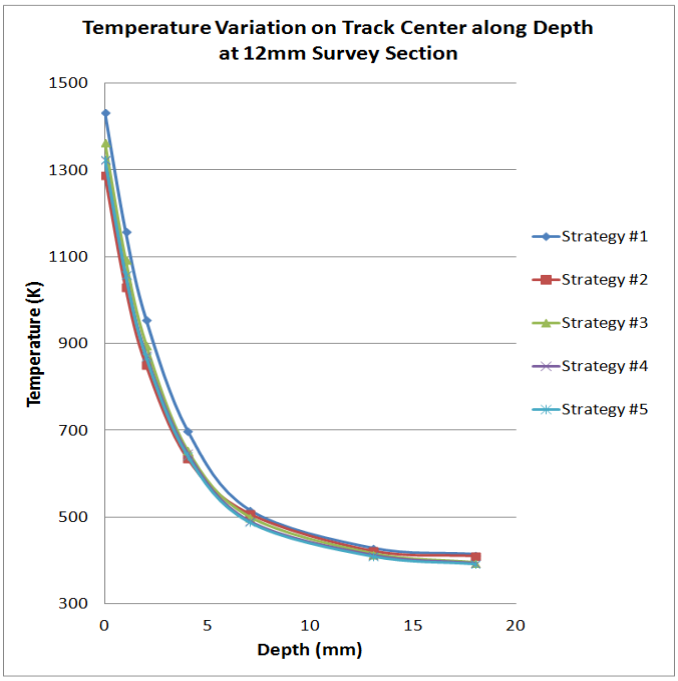

Figure 11. Temperature Variation on Surface Points at 40mm Survey Section.

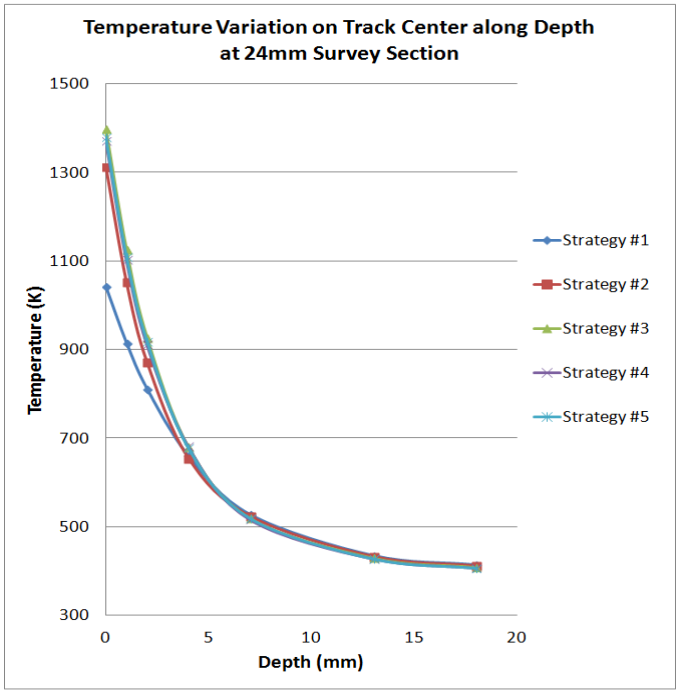

Figure 12. Temperature Variation on Surface Points at 40mm Survey Section.

Figure 13 shows that strategy #1 results in the lowest temperature and strategy #2 the highest temperature at all nodes at section 40mm. The other strategies result in values between the two. It can also be observed that strategies #3, #4 and #5 reported almost similar results for all nodes, and very close to that of strategy #2. With strategy #5 as the baseline model, on the 40mm section, a maximum difference of 0.6% for strategy #4, 1.3% for strategy #3, 3.4% for strategy #2, and 22.6% for strategy #1 was calculated. The unexpected trend in figure 13 at a depth of about 13-14mm is the heat accumulation at the survey node.

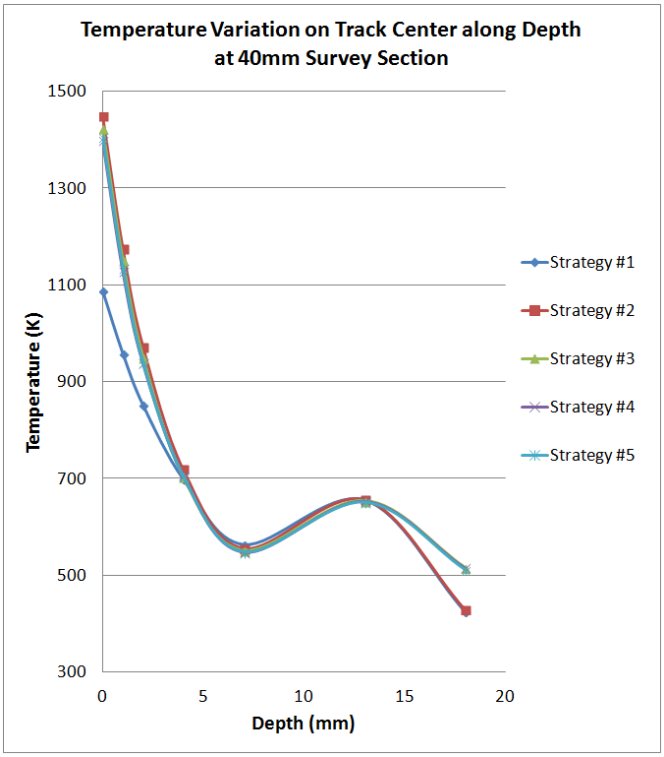

Figure 13. Temperature Variation on Surface Points at 40mm Survey Section.

Figures 14, 16 and 18 show the final thermal stress (as the part cools back down to room temperature, residual stress) variation on the survey points (a, b, c, d, e, f, g, h and i) on the plate surface (a) along the laser direction and (b) transverse direction to the laser traverse on sections that are 12mm, 24 mm and 40mm away from the starting plate edge (front edge in figure 7), respectively. Figures 15, 17, and 19 show the variation of final thermal stress on the survey points (a, j, k, l, m, n and o) in the depth direction (a) along the laser direction and (b) transverse direction to the laser traverse on section that are 12mm, 24 mm and 40 mm away from the starting plate edge, respectively. Since the nodal stresses are symmetric about the plane of center track (normal to the plate top surface) only half plate nodal stresses at the survey sections have been reported.

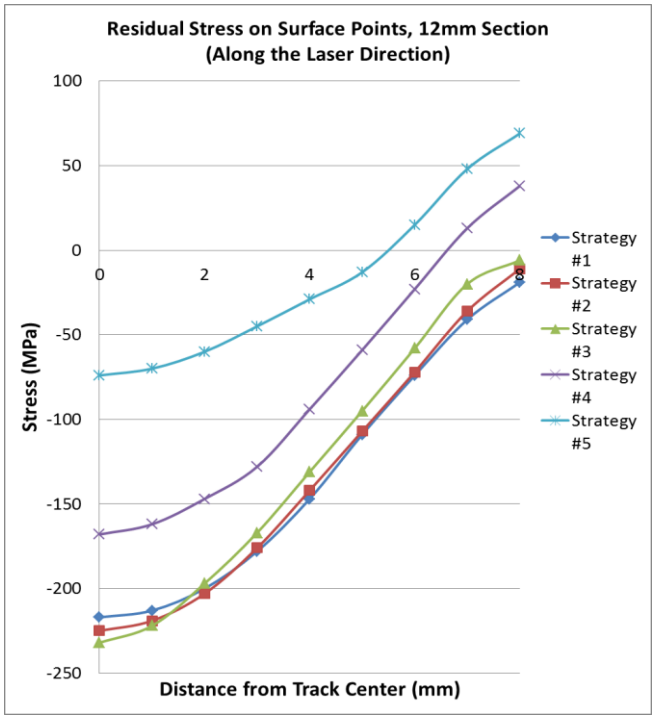

(a)

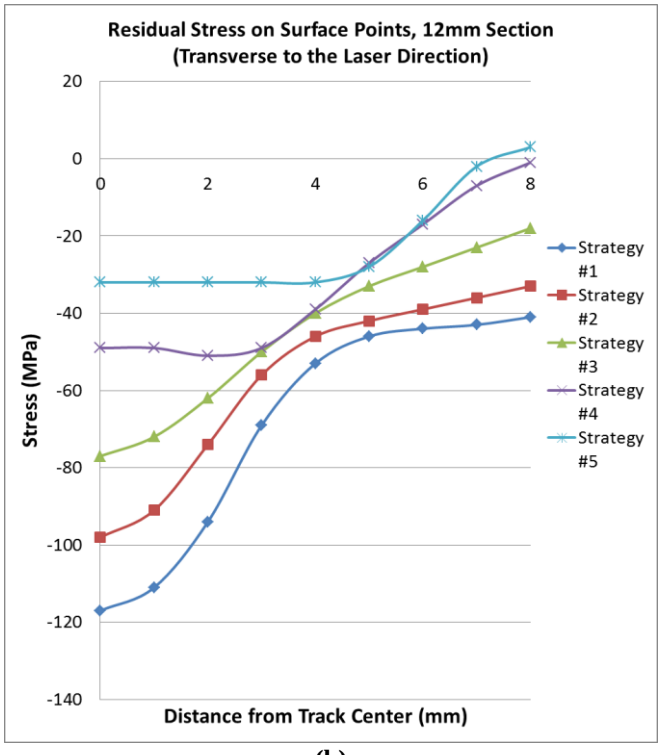

(b)

Figure 14. Residual Stress Variation on Surface Points (a) along the direction and (b) transverse to laser travel direction at 12mm Survey Section.

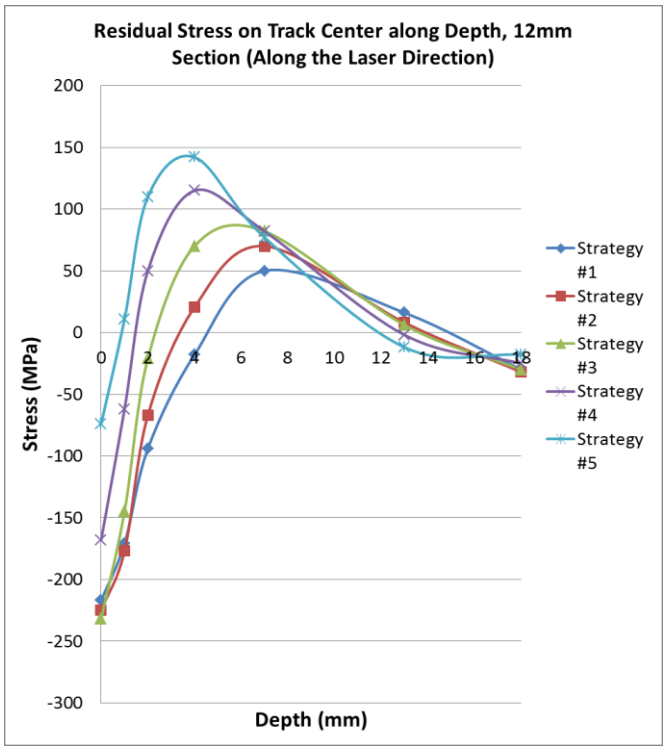

(a)

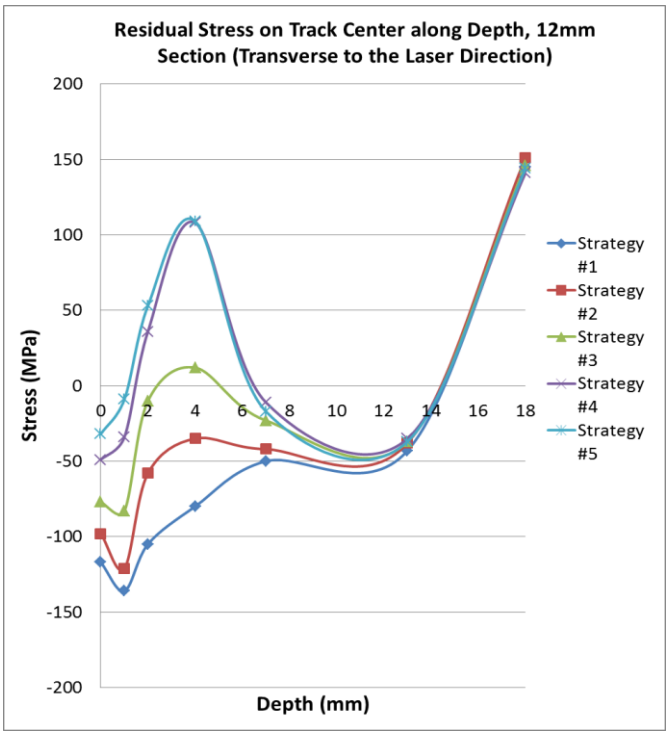

(b)

Figure 15. Residual Stress Variation on Track Center (a) along the direction and (b) transverse to laser travel direction at 12mm Survey Section.

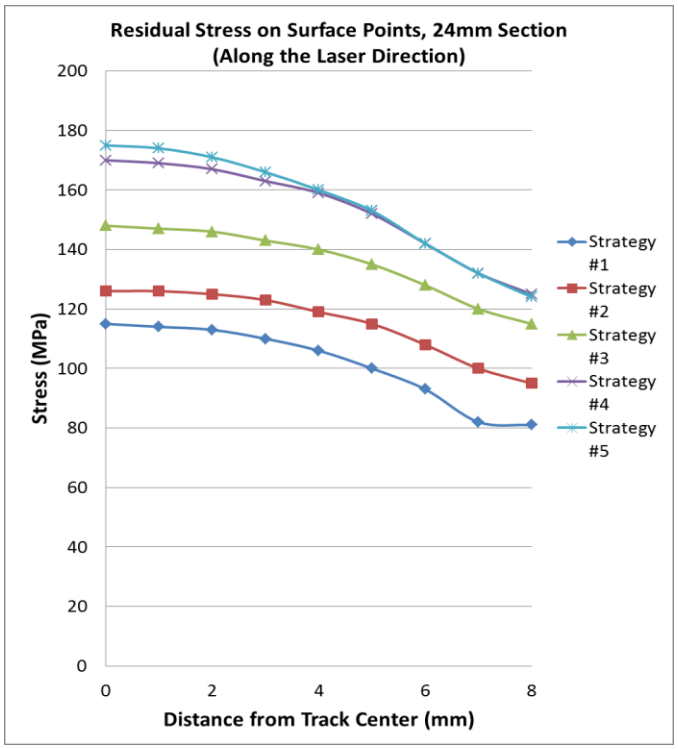

(a)

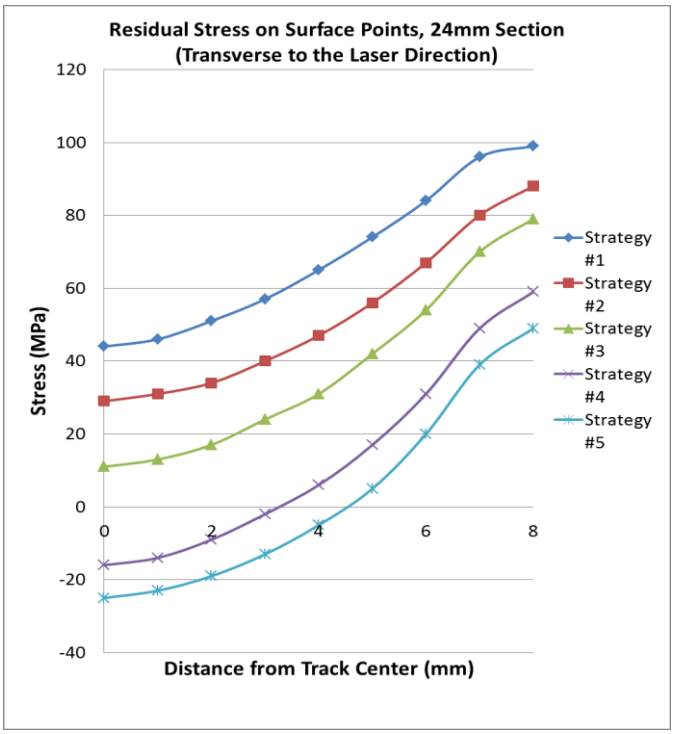

(b)

Figure 16. Residual Stress Variation on Surface Points (a) along the direction and (b) transverse to laser travel direction at 24mm Survey Section.

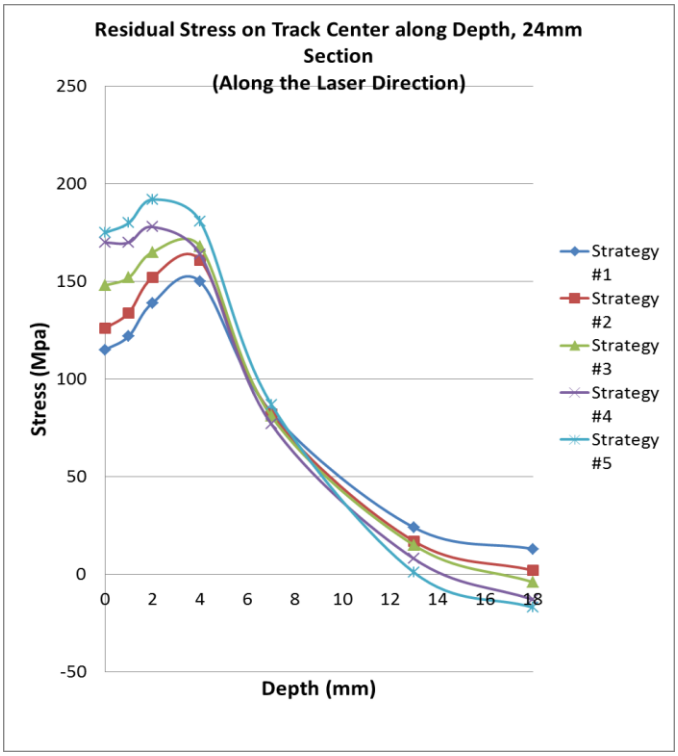

(a)

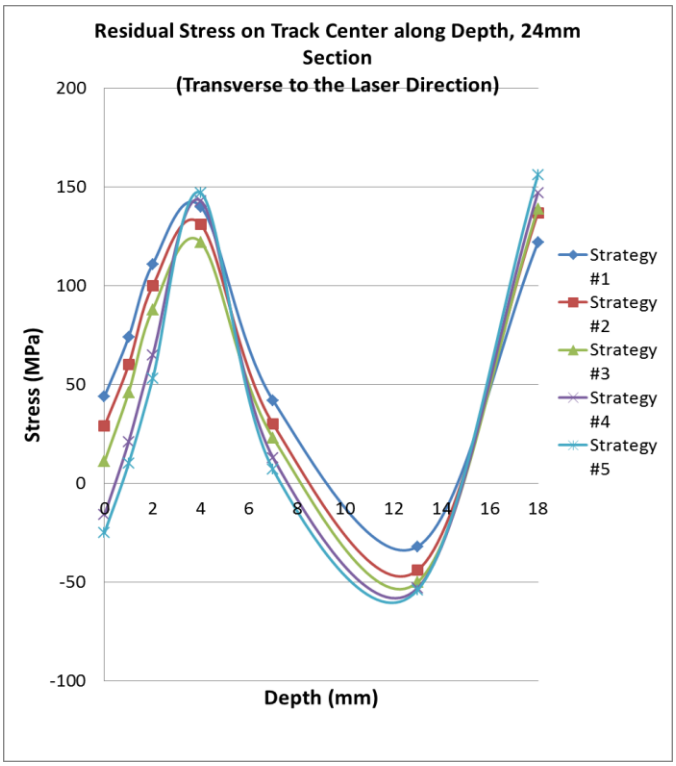

(b)

Figure 17. Residual Stress Variation on Track Center (a) along the direction and (b) transverse to laser travel direction at 24mm Survey Section.

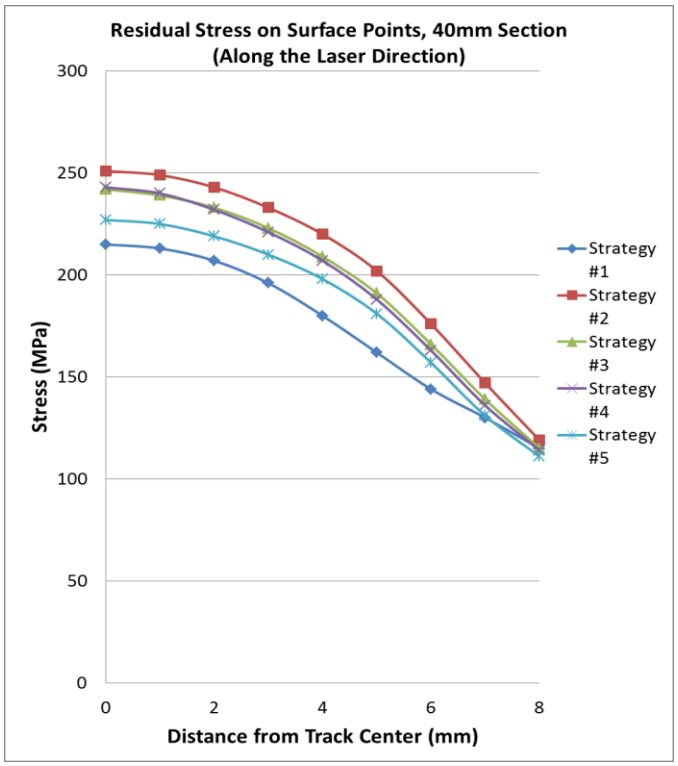

(a)

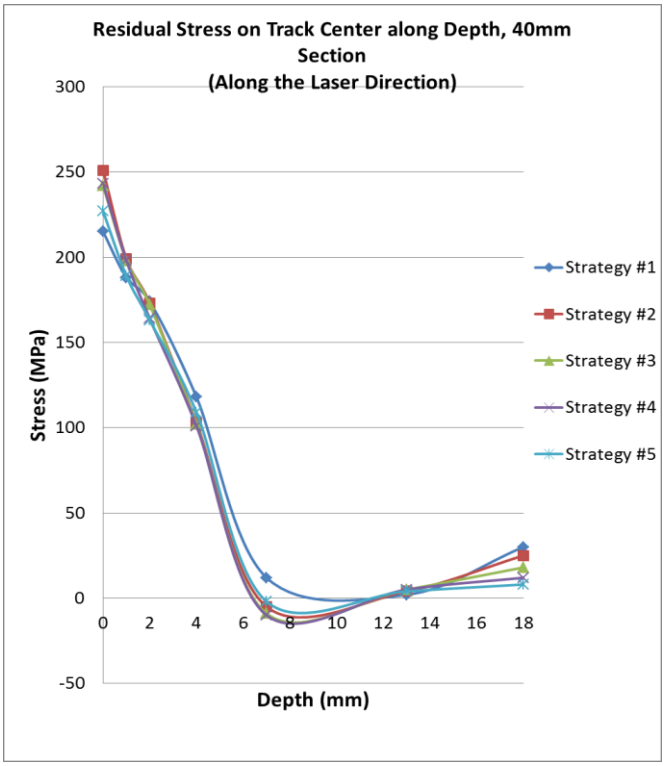

(a)

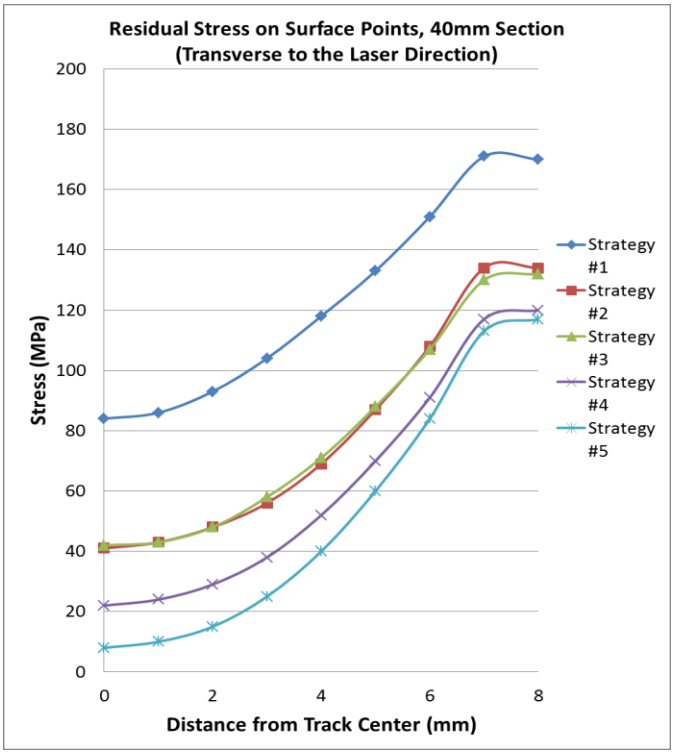

(b)

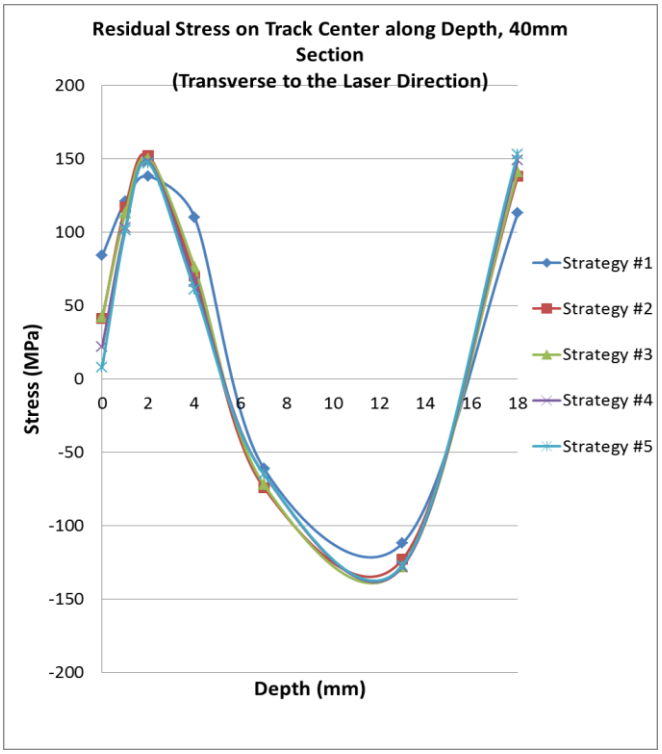

(b)

Figure 18. Residual Stress Variation on Surface Points (a) along the direction and (b) transverse to laser travel direction at 40mm Survey Section.

Figure 19. Residual Stress Variation on Track Center (a) along the direction and (b) transverse to laser travel direction at 40mm Survey Section.

As expected, at the 12 mm section, the thermal stresses (both along the laser travel and transvers to laser travel directions) are highest compressive at the laser track center, and it drops consistently away from the center line, becoming less compressive (or tensile in some cases). Strategies #1, #2 and #3 reported similar results along the direction of laser, however, strategy #2 was the only one that came close to strategy #1 with a 20% maximum difference in the transverse direction to laser travel. It is also interesting to notice that strategies #1, #2 and #3 report similar results on the laser track center (in both along and transverse directions), but start deviating as we march in the depth direction. The maximum difference in all strategies from strategy #1 is observed at a depth of nearly 4 mm. This deviation reduces again as we march further than 4 mm in the depth direction.

Similar to the temperature results, at the 24 mm and 40 mm sections, all strategies deviated a lot in their thermal stress results from strategy #1 on the surface points, both along and transverse to the laser travel direction. However, it is very interested to observe that at the same cross sections (24 and 40 mm), the strategies showed similar results to each other at the laser track center and points underneath in the depth direction, both along and transverse to the laser travel direction.

Table 1 shows the total computational time taken for temperature and thermal stress runs (analyses) in each strategy.

Table 1. Computational Times for Different Strategies

Strategy	CPU Time (seconds)		Total Wall Clock Time (seconds)	
	Temperature Run	Stress Run	Temperature Run	Stress Run
#1	1645	5153	6027	19767
#2	1964	5435	7372	22673
#3	2333	6848	8477	29195
#4	3086	15275	7832	32009
#5	3867	24775	8439	77910

Again, with strategy #5 as the baseline model, strategy #4 has a CPU time savings of 20.2%, strategy #3 39.7%, strategy #2 49.2% and strategy #1 time savings of 57.5%. for the temperature runs. Similarly, strategy #4 has a CPU time savings of 38.3%, strategy #3 72.4%, strategy #2 78.1% and strategy #1 time savings of 79.2%. for the thermal stress runs.

Based on the variations of temperatures on these different survey sections, both along transverse and depth directions, one can now settle on a trade-off between accuracy of temperatures and computational times. The analyses in most of our cases lead to believe that strategies #3, #4 and #5 will provide the best and closest results. Further, strategy #3 provided the highest deviation of 4.9% in any of these cases put together. This can easily be outweighed by the time savings of nearly 40%. A substantial time savings can be observed for the same strategies for the thermal runs. Further, effect of process variables (viz., laser power, size and speed) must also be investigated to determine a range of load step selections for process optimization.

CONCLUSIONS

In this paper the effects of different modeling strategies for laser travel on the prediction of temperature transient response and distribution was explored. These results showed that a significant gain in simulation times can be achieved by a marginal compromise on the accuracy of results. To maintain the quasi-steady state nature of heat flow through the plate, and to achieve these results within the smallest computational times, one need not move the laser in the smallest time increments (or load steps). A prudent choice of time/load steps based upon an overlap of nearly 70 to 85% in the heat flux in the successive steps will optimize the simulation process. These savings in computational times accrue for large area laser hardening processes in which multiple laser passes are needed to scan the whole area. However, suggested 70 to 85% overlap in heat flux to simulate relatively higher than the smallest time/load steps should be researched further for different scanning paths, viz. raster zig-zag, raster unidirectional, spiral in-to-out or spiral-out-to-in as they can lead to different conclusions for phase transformation stresses as compared to thermal stresses in general [20].

REFERENCES

[1] Pantelis, D.I., Bouyiouri, E., Kouloumbi, N., Vassiliou, P., and Koutsomichalis, A., 2002, "Wear and Corrosion Resistance of Laser Surface Hardened Structural Steel," Surface and Coatings Technology, 298, pp. 125-134.

[2] Molian, P.A., and Baldwin, M., 1987, "Effects of Single-pass Laser Heat Treatment on Erosion Behavior of Cast Irons," Wear, 118, pp. 319-327.

[3] Peng, R.L., and Ericsson, T., 1998, "Effect of Laser Hardening on Bending Fatigue of Several Steels," Scandinavian J. Metallurgy, 27, pp. 180-190.

[4] Doong, J.L., Chen, T.J., and Tan, Y.H., 1989, "Effect of Laser Surface Hardening on Fatigue Crack Growth Rate in AISI 4130 Steel," Engineering Fracture Mechanics, 33, pp. 483-491.

[5] Sridhar, K., and Khanna, A.S., 1998, "Laser Surface Heat Treatment," Lasers in Surface Engineering: Surface Engineering Series ASM International 1, pp. 69-119.

[6] Pashby, I.R., Barnes, S., and Bryden, B.G., 2003, "Surface Hardening of Steel using a High Power Diode Laser," Journal of Materials Processing Technology, 139, pp. 585-588.

[7] Ion, J.C., 2002, "Laser Transformation Hardening: Review," Surface Engineering, 18, pp. 14-31.

[8] S. Kou, D.K. Sun, Y.P. Lee, A fundamental study of laser transformation hardening, Metallurgical Transactions A 14 (1983) 643-653.

[9] M. Davis, P. Kapadia, J. Dowden, W.M. Steen, C.H.G. Courtney, Heat hardening of metal surfaces with a scanning laser beam, Journal of Physics D 19 (1986) 1981-1997.
[10] A. Yanez, J.C. Alvarez, A.J. Lopez, G. Nicolas, J.A. Perez, A. Ramil, E. Saavedra, Modelling of temperature evolution on metals during laser hardening process, Applied Surface Science 186 (2002) 611-616.
[11] R. Komanduri, Z.B. Hou, Thermal analysis of the laser surface transformation hardening process, International Journal of Heat and Mass Transfer 44 (2001) 2845-2862.
[12] M.F. Ashby, K.E. Easterling, The transformation hardening of steel surfaces by laser beams – I: Hypoeutectoid steels, Acta Metallurgica 32 (1984) 1935-1948.
[13] E. Ohmura, K. Inoue, Y. Takamachi, Theoretical analysis of laser transformation hardening process of hypoeutectoid steel based on kinetics, JSME International Journal Series I 34 (1991) 421-429.
[14] Dong Lin, C Ye, Y Liao, S Suslov, C. R. Liu, G. J. Cheng, "Laser shock peened TiN nanoparticle integrated AISI 4140 and its mechanical properties improvement", Journal of Applied Physics, 2013, 113, 133509.
[15] Ghosh, S., and Choi, J., 2005, "Three-Dimensional Transient Finite Element Analysis for Residual Stresses in the Laser Aided Direct Metal/Material Deposition Process," Journal of Laser Applications, 17(3), pp. 144-158.
[16] Incropera, DeWitt, Bergman, Lavine, 2007, *Fundamentals of Heat and Mass Transfer*, John Wiley & Sons, Hoboken, NJ. pp72. Chap2.
[17] Ghosh, S., Sahay, C., and Connors, J., 2013, "Comparative Study between FEA-based Sequentially-Coupled and Fully-Coupled Thermal Stress Models in a Laser Hardening Process," Proceedings of the ASME International Mechanical Engineering Congress & Exposition, IMECE2013-63745, November 13-21, San Diego, CA.
[18] Safdar, S., Li, L., Sheikh, M.A., Schmidt, M.J., 2006, "Thermal History Analysis of Surface Heating of Mild Steel with Different Laser Beam Geometries", Journal of Mechanical Engineering Science, 220, pp. 1547-1557.
[19] Touloukian, Y.S. & Ho, C.Y. (1970) Thermo physical properties of matter-The TPRC Data Series by Purdue University, IFI/Plenum Data Corp., New York.
[20] Ghosh, S., and Choi, J., 2007, "Deposition Pattern Based Thermal Stresses in Single-Layer Laser Aided Direct Material Deposition Process," ASME Journal of Manufacturing Science and Engineering, 129(2), pp. 319-332